High-Energy Quasiparticle Injection in Mesoscopic Superconductors

L. D. Alegria,[1] C. G. Bøttcher,[1] A. K. Saydjari,[1] A. T. Pierce,[1] S. H. Lee,[1] S. P. Harvey,[2] U. Vool,[1] and A. Yacoby[1]

[1]*Department of Physics, Harvard University, Cambridge, Massachusetts 02138*

[2]*Department of Physics, Stanford University, Stanford, California 94025*

(Dated: May 5, 2020)

Abstract

At nonzero temperatures, superconductors contain excitations known as Bogoliubov quasiparticles. The mesoscopic dynamics of quasiparticles are crucial to designing quantum information processors, among other devices. Knowledge of these dynamics stems from experiments in which quasiparticles are injected in a controlled fashion, typically at energies comparable to the superconducting energy gap[1–5]. Here we perform tunnel spectroscopy of a mesoscopic superconductor under high electric field. We observe quasiparticle injection into titanium with 10^6 times the gap energy, an unexplored regime of quasiparticle dynamics. We expect that high-energy injection will be useful for developing quasiparticle-tolerant quantum information processors, will allow rapid control of resonator quality factors, and will enable the design of electric-field-controlled superconducting devices with new functionality.

I. MAIN

Traditional superconducting information processing devices are actuated by substantial currents ($\gtrapprox \mu$A), including cryotrons[6], transmons[7], single flux quantum processors [8], and others[9, 10]. The challenges of scaling transmon-style qubits to useful numbers of bits motivate recent work to actuate superconductivity by electric field effects, such as depletion of a proximally superconducting semiconductor[11]. But, for resonator devices, almost any added semiconductor layer deteriorates the quality factor of the device[12]. A simpler solution seemed improbable[13] until recently, when a field effect on the critical current of metallic superconducting nanowires was described [14], but not satisfactorily explained.

In this Letter, we examine the effect of high electric fields on mesoscopic superconductors by colocating a gate electrode and a local tunnel probe. As compared to the previous critical current measurements, tunnel spectroscopy provides a static measurement that can access the details of the electronic states, and, in the case of a superconductor, specifically measures the quasiparticle (QP) population[15]. We find that the electric field from the gate introduces a QP current via field emission. The high energy ($\sim$ 40 eV) of the current explains its efficiency at disturbing the superconducting state and its prior non-detection.

Quasiparticle dynamics have long been a subject of fundamental inquiry. Early studies observed how QP recombine, emitting phonons which can excite further QP until the phonons escape[1, 2]. More recently, the non-galvanic propagation of QP via phonons has been spatially quantified using resonators as detectors[5]. Accelerating progress in quantum information has made QP dynamics a critical topic, as their often-uncertain populations may limit the performance of quantum processors[16]. In such circuits, the significant presence of high-energy and even cosmogenic QP has prompted recent use of radioisotopes as experimental sources of QP[17]. In addition to applications in quantum information, the cascading of energetic QP underpins the operation of superconducting particle detectors[18], and recent interest in microfabricated particle accelerators may ultimately present opportunities for high-energy superconducting microelectronics[19]. A conveniently fabricated, high-energy QP source is therefore of practical and fundamental interest.

We fabricate the device shown in Figure 1a via electron-beam lithography and in-situ double-angle shadow evaporation. We deposit and oxidize a 10 nm thick Al film to form a

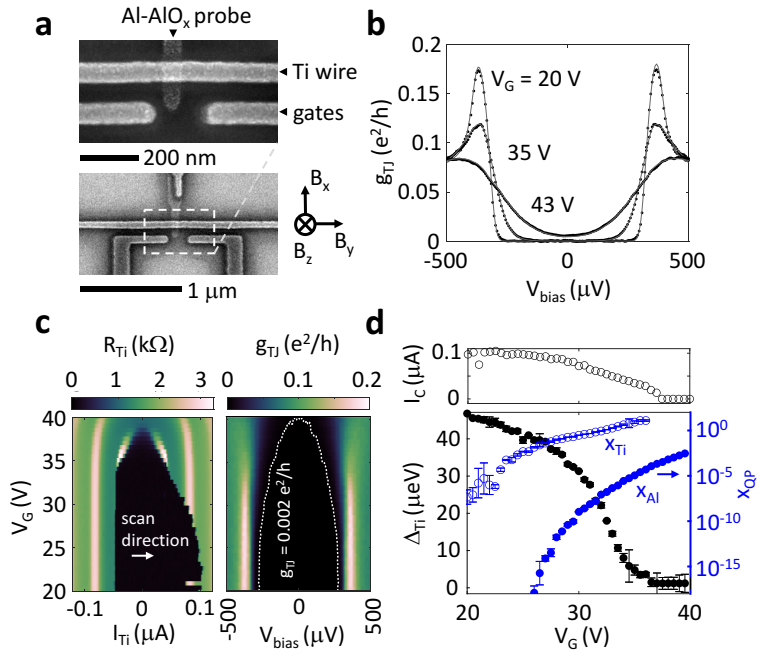

FIG. 1: Tunnel spectroscopy and critical current of a titanium nanowire at high gate voltage (V_G) and 20 mK temperature. (a) Electron micrograph of the device, which consists of a titanium wire, local surface gates, and an aluminum tunnel probe. (b) Example tunnel data (dots) and fitted Abrikosov-Gorkov model (lines) at the indicated gate voltages. (c) Wire resistance versus current (left) and tunnel spectrum (right) as functions of the applied gate voltage. (d) Gate dependence of the critical current (I_C) as compared to the quasiparticle fraction ($x_{\mathrm{QP}} = n_{\mathrm{QP}}/n_{\mathrm{Cooper\ pairs}}$) and the titanium superconducting gap (Δ_{Ti}) inferred from the fitted model. The rise in quasiparticle density indicates quasiparticle injection as the mechanism for the observed suppression of the critical current in gated metallic superconductors.

tunnel probe, followed by a 30 nm thick Ti film to form a 60 nm wide nanowire channel and nearby gates. The nanowire and probe extend to contacts, allowing both critical current and tunnelling measurements of the Ti channel while the voltage on the gate electrodes is varied.

Figure 1c shows the critical current and tunnel conductance of the Ti wire as a function of applied gate voltage, measured at 20 mK. We measure the resistance of the Ti wire as the current is swept from negative to positive values, entering and exiting the zero resistance state at the retrapping and critical current (I_c) respectively. Application of gate voltage

decreases the critical current before completely eliminating superconductivity, consistent with the results of [14]. In the same device and gate range, we measure the tunnel spectrum, as shown in the right hand of Figure 1c. The results are illuminating: the spectrum broadens dramatically with gate voltage, implying a rapid increase of the QP population.

We analyze the data using a conventional model for tunnel spectroscopy. Tunneling from superconductors can reveal the electronic, magnetic, and phonon structure of materials due to the highly non-linear superconducting density of states[15, 20, 21]. The current through a tunnel junction is given by

$$I_{\mathrm{TJ}} = \frac{g_0}{N_1^{(0)} N_2^{(0)}} \int N_1(E) N_2(E + eV_{\mathrm{bias}})(f(E) - f(E + eV_{\mathrm{bias}}))dE \tag{1}$$

where g_0 is the normal-metal conductance, $N_{1,2}(E)$ are the densities of states for each side of the junction, $N_{1,2}^{(0)}$ are the normal-metal densities of states, V_{bias} is the bias voltage on the tunnel probe, and $f(E) = (1+\exp(E/k_B T_{\mathrm{QP}}))^{-1}$ is the Fermi function, which defines the QP temperature, T_{QP}. The magnetic field serves as a convenient experimental parameter, in the presence of which each density of states is split into spin subbands, $N_{\uparrow\downarrow}$, treated separately in the limit of low spin-flip scattering, and given in the Abrikosov-Gorkov model [22] as

$$N_{\uparrow\downarrow} = \frac{N^{(0)}}{2} \mathrm{sgn}(E) \mathrm{Re}\left(\frac{u_\pm}{(u_\pm^2 - 1)^{1/2}}\right) \tag{2a}$$

$$u_\pm = \frac{E \mp \mu_B B}{\Delta} + \alpha \frac{u_\pm}{(1 - u_\pm^2)^{1/2}} \tag{2b}$$

where $u_\pm$ are defined implicitly, μ_B is the Bohr magneton, B is the external magnetic field, Δ is the superconducting gap, and α is the depairing energy. The depairing energy reflects the typical energy difference between time-reversed electron states. The functions $N_{(\mathrm{Al,Ti})(\uparrow,\downarrow)}(E)$ can be obtained analytically by solving equation (2b) for the $u_\pm$. The total current for both spin channels is then calculated numerically according to equation (1), and the derivative with respect to V_{bias} gives the conductance

$$g_{\mathrm{TJ}}(V_{\mathrm{bias}}) = \left.\frac{dI_{\mathrm{TJ}}}{dV_{\mathrm{bias}}}\right|_{\Delta_{\mathrm{Al}}, \Delta_{\mathrm{Ti}}, \alpha_{\mathrm{Al}}, \alpha_{\mathrm{Ti}}, B, T_{\mathrm{QP}}} \tag{3}$$

for given gap energies, depairing energies, magnetic field, and quasiparticle temperature. Moreover, in the approximation that the two layers of the junction are in thermal equilibrium, we can calculate the QP fraction for either layer, $x = \int N(E)f(E)dE/(N^{(0)}\Delta)$. This value is defined as the ratio between the density of occupied excited states, $\int N(E)f(E)dE$, and the density of Cooper pairs, $N^{(0)}\Delta$ [23].

With this model we return to the data of Figure 1b-c. The tunnel conductance depends on the convolution of the Al and Ti densities of states, causing a peak at the sum-of-gaps. The peak in Figure 1c does not move greatly when I_C becomes zero at $V_G = 37$ V, which illustrates that the Al gap is much larger than the Ti gap.

We fit the model of equation (3) to the data of Fig 1c, taking $T_{\rm QP}$ and $\Delta_{\rm Ti}$ as free parameters, and fixed $\Delta_{\rm Al} = 320$ μeV[24]. The resulting $\Delta_{\rm Ti}$ correlates with the measured critical current as plotted in Figure 1d. We also plot the resulting QP fraction in the Al and Ti layers. Given the accuracy of the fit (see Figure 1b) the smooth rise in QP population indicates that QP injection, rather than a change in the underlying electronic or crystal structure, is responsible for the suppression of superconductivity.

Still, it might be argued that a magnetic mechanism may lead to broadening like that observed with application of V_G. For instance, under high electric fields, oxygen ions might accumulate and present a large moment at the surface of the Ti [25, 26].

Figure 2 explores the effects of magnetic field to characterize the material system and consider the possibility of a magnetic gating effect. Figure 2a shows the spectrum at several values of magnetic field. The model accurately captures the orbital depairing and Zeeman splitting. The critical current data (Figure 2b, left) show a critical magnetic field in the Ti at $B_x = 0.7$ T, and inspection reveals a discontinuity at this field in the respective tunnel data (Figure 2b, right). To make quantitative conclusions, we fit the model to the tunneling data as follows. We first consider the region 1 T $< B_x <$ 2.5 T, in which the Ti is normal, and the Al superconducting. Here, the model has free parameters $\Delta_{\rm Al}$ and $\alpha_{\rm Al}$ which follow quadratic trajectories shown as dashed lines in Figure 2c ($T_{\rm QP} = 20$ mK). These trajectories are used to fit the low-field region, where only $\Delta_{\rm Ti}$ and $\alpha_{\rm Ti}$ are taken to be free parameters. The resulting Ti parameters also follow quadratic dependences, and from the relation $\alpha = (eH_\parallel^2 d^2/6\hbar + H_\perp)De/c$ for a thin film of thickness d, we find the diffusion constants $D_{\rm Al} = 0.6$ cm^{2}s^{-1} and $D_{\rm Ti} = 2.4$ cm^{2}s^{-1} as well as a 2.5 degree field misalignment[23]. The low diffusion constants are consistent with the large density of

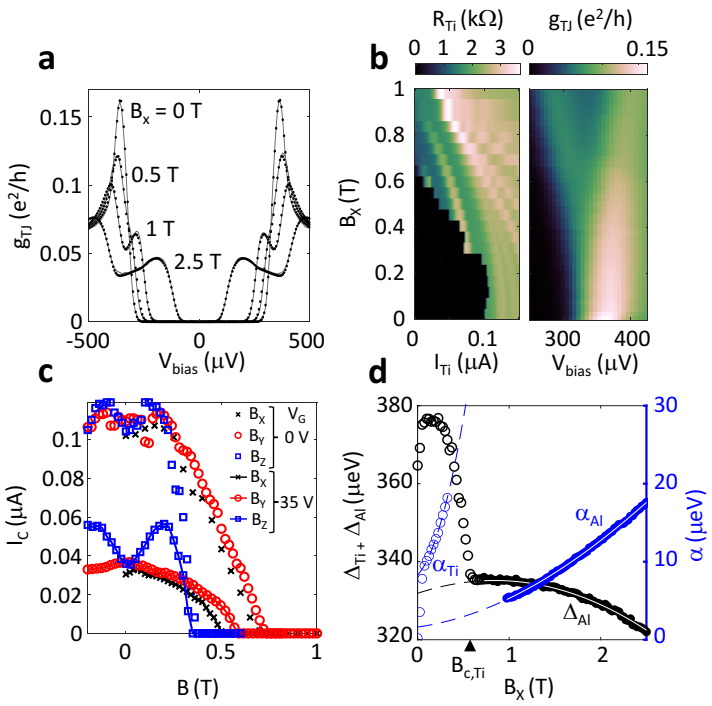

FIG. 2: Device characterization in applied magnetic field. (a) Example tunnel data (dots) and fits (lines) with magnetic field applied along the x-axis, illustrating the Zeeman splitting of the density of states and the depairing effect, which is distinct from the effect of quasiparticle injection. (b) Comparison of the titanium resistance (left) and the tunnel spectrum (right) as functions of the magnetic field. (c) Titanium critical current under x, y, and z field orientations, both at zero and elevated gate voltage. (d) The gap and depairing energies ($\Delta_{\mathrm{Al,Ti}}$, $\alpha_{\mathrm{Al,Ti}}$,) obtained by fitting the tunnel data above (filled circles) and below (open circles) the titanium critical field ($B_{\mathrm{c,Ti}}$) as described in the text.

scattering sites typical in these thin polycrystalline metal films[24]. Further, Figure 2c shows the critical current for magnetic fields along all device axes and for both zero and high gate voltage, illustrating the predominantly isotropic nature of the gate effect (complete data in Figure S1). If we try to account for the broadening due to the gate (Figure 1b) with the depairing parameter α rather than T_{QP}, the fit is far worse (see Figure S2). Strictly speaking, by distinguishing between the effect of magnetic fields (α) and the effect of the gate voltage (T_{QP}) we not only rule out magnetic effects, but any ergodic pair-breaking origin of the gate effect [23].

Next, in Figure 3a, we apply a fixed field $B_x = 2$ T such that the Ti is in the normal

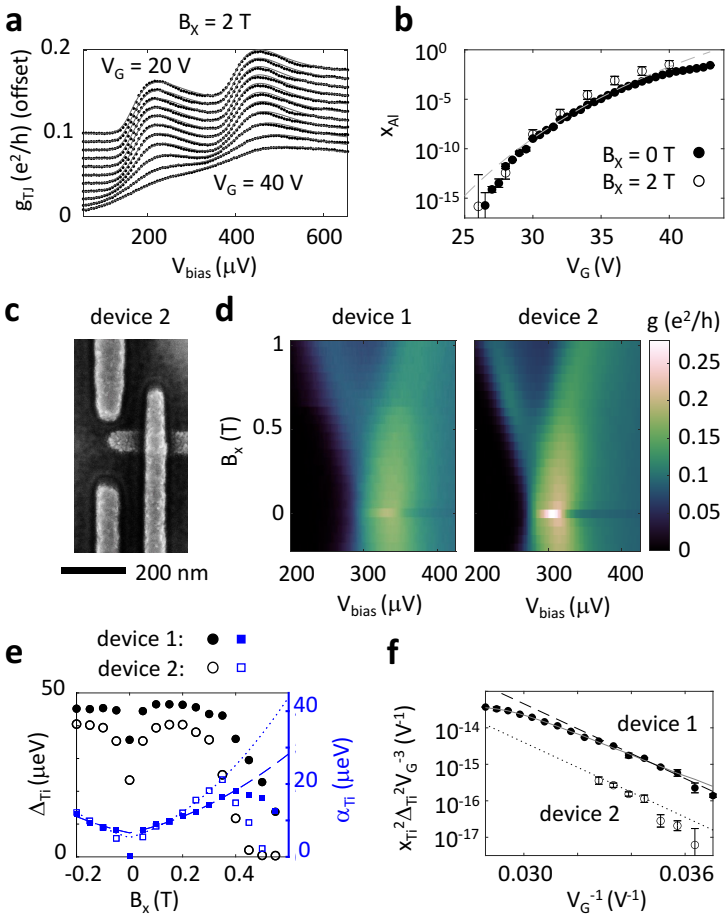

FIG. 3: Injection in fixed high magnetic field, a second device, and a model of quasiparticle injection due to field emission. (a) Tunnel spectrum vs V_G at fixed $B_x = 2$ T, well above the titanium critical field. (b) The calculated quasiparticle fraction x within the aluminum for $B_x = 2$ T (open circles), $B_x = 0$ (filled circles), and the function $a\exp(-V_0/V_G)$ (dashed line). (c) A second, 'tunneling-only' device displaying a sharper spectrum (d) but similar magnetic field (e) and gate voltage dependences to the first device. (f) The observed quasiparticle fraction is largely explained by a simple model of quasiparticle dynamics assuming Fowler-Nordheim emission from the gate (dashed and dotted lines). A more detailed model (grey curve) incorporates one-dimensional diffusion away from the injection region.

state, and then apply gate voltage. These data admit simpler analysis: with the Ti normal, equation (3) reduces to $g_{\rm TJ}(V_{\rm bias}) \sim \int N_{Al}(E - eV_{\rm bias})f'(E - eV_{\rm bias})dE$. So we are simply looking at the thermally-broadened Al density of states. The observed broadening with V_G confirms the hypothesis of QP generation, and is largely independent of applied magnetic

field.

We now note two key differences between this experiment and classical QP injection experiments[1–3]. First, the injected QP begin at energies ($\approx eV_G$) inaccessible to the spectroscopy, and, second, the current is so low in our case it can be difficult to measure. Even without direct measurements of the current we can examine $x(V_G)$ for clues to the underlying transport mechanism. We plot $\log(x_{\rm Al}(V_G))$ in Figure 3b, as calculated from the data of Figure 3a and 1c. With or without strong magnetic field, the Al data roughly follow $x \sim \exp(-V_0/V_G)$ for $V_0 = 2$ kV, which suggests field emission. But, in our geometry, current from the gate most directly enters the Ti. Consequently, we focus on the QP population in the Ti within the following simple kinetic model.

Given an injection current I_G the number of QP in the Ti portion of the device is approximately

$$n_{\rm QP} = \frac{I_G V_G \tau_{\rm eff}}{\Delta} \tag{4}$$

where $\tau_{\rm eff} = \tau_0/x$ is the effective QP lifetime[1, 4]. That is, each electron from the gate excites roughly V_G/Δ thermal quasiparticles which decay in proportion to their density due to recombination. In terms of x, the value $n_{\rm QP} = x\Omega N^{(0)}\Delta_{\rm Ti}$, where Ω is the volume of the Ti injection region. The current between two metals separated by a vacuum can be calculated from the Fowler-Nordheim equation, $I = aV^2 \exp(-b/V)$. Here $a = eS/(16\pi^2\hbar\phi l^2)$ and $b = 4l(2m\phi^3)^{1/2}/(3\hbar)$ with S the emission area, ϕ the work function, and l the separation[27]. Substituting into equation (4), we expect the following approximate relation:

$$\frac{x^2\Delta^2}{V_G^3} = Ae^{-b/V_G} \tag{5}$$

with $A = a\tau_0/(N^{(0)}\Omega)$. In Figure 3f, we plot the left-hand quantity (from the data of Figure 1c) on a log scale versus V_G^{-1} and find a nearly linear dependence. The dashed line corresponds to $l = 33$ nm and $\phi = 2.3$ eV. The value of $A = 6 \times 10^{-4}$ V^{-1} accords with the realistic estimates $\tau_0 = 5$ ns, $S = 30$ nm $\times$ 0.6 μm, $N^{(0)} = 7 \times 10^{10}$ μm^{-3}eV^{-1}, $\Omega = 4$ μm $\times$ 60 nm $\times$ 30 nm, validating the field emission hypothesis and indicating that the current impinges on the superconductor with the energy of the electrode. A model taking into

account QP diffusion along the wire is described in figure S3, and captures the nonlinearity in Fig 3f. A more sensitive measurement of the current, inclusion of multiple detectors, and a wider spectroscopy could all elucidate the injection and equilibration process.

To confirm the results, we also study a second device in Figure 3c, which is similar to the first except that the Ti wire is terminated on one side. In Figure 3d we compare $g(V_{\rm bias}, B)$ of the two devices and attribute the comparative sharpness of the second device to microscopic differences in the films. The results of fitting the tunnel data in applied magnetic field and electric field are similar to those of the first device (Figure 3e-f). The higher diffusion constant, $D_{\rm Ti} = 3.2$ cm^{2}s^{-1}, in the second device may contribute to its having a lower A parameter ($A = 6 \times 10^{-5}$ V^{-1}). In addition, several devices with simpler geometries were measured at dilution refrigerator temperatures in order to directly reproduce the results of [14]. Devices gated through SiO_2 exhibit similar effects, but with hysteresis pointing to ionic transport (see Figure S4). In all devices, the effect is found to be stable over week-long time-scales.

II. CONCLUSION

With sufficient electric field, mesoscopic superconductors can be switched into the normal state with low quiescent currents. By introducing a tunnel junction, we have directly observed the QP injection mechanism which governs the phenomenon. The mechanism may be suited as a generally applicable switch of superconductivity, since field emission implies that little dissipation occurs outside of the channel region, in contrast to prior three-terminal superconducting devices[9].

The finding may be especially relevant to superconducting quantum information processors. Such processors suffer from costly scaling for useful numbers of qubits and, more fundamentally, insufficient coherence of individual qubits. The gate effect suggests a new approach to the former problem: a gate-tuned resonator would have circuit design advantages so long as the QP population is tolerable. Just how many QP are tolerable remains an open question, and one which a high-energy QP injector may help investigate. Since high-energy QP are a little-understood source of decoherence, new designs of QP-absorbing traps could be tested by interposition between the high-energy QP source and a detector qubit.

III. METHODS

The devices are fabricated beginning with a bilayer resist (950 kDa PMMA, 4% in anisole, on (MMA (8.5) MAA) copolymer, 11% in ethyl lactate) on dry-oxidized (90 nm), degenerately doped (001) Si, which is exposed using a 150 kV electron beam pattern generator to create a suspended mask. 10 nm of Al is thermally evaporated at 30 degrees from normal incidence and oxidized in 100 Torr medical grade air for 30 min, after which 30 nm Ti is deposited at normal incidence. The devices are cleaned by UV-ozone treatment (Samco UV-1, 40 deg C, 3 min) after acetone liftoff. The zero-field values of the gaps, $\Delta_{\mathrm{Al},0} = 320$ μeV and $\Delta_{\mathrm{Ti},0} = 50$ μeV, are consistent with typical enhancement of superconductivity in environmentally exposed Al films and degradation of Ti relative to bulk materials ($\Delta_{\mathrm{Al,bulk}} = 180$ μeV and $\Delta_{\mathrm{Ti,bulk}} = 75$ μeV)[24]. The diffusion constants measured in the main text correspond to mean free paths $l \approx 3D/v_{\mathrm{F}}$ of 1 - 5 Å, consistent with near-unity residual resistance ratios in these films ($\mathrm{RRR_{Ti}} = 1.3$, $\mathrm{RRR_{Al}} = 1.05$) [24, 28]. Four terminal measurements of the devices are performed in a dilution refrigerator at 17 - 22 mK equipped with low-temperature low-pass filtering, using a Keithley 2400 as gate voltage source. In order to tolerate a slight misalignment in the shadow evaporation process, the gate voltage is applied to the right hand gate in figure 1a, as detailed in Figure S5.

To model a given sequence of tunneling data (g_{TJ} versus either B or V_G), 400 random initial points in the parameter space are taken, from each of which a gradient descent is performed. The objective function is calculated with 0.1 μeV resolution from equation (3). Subsequent fits start from 100 initial parameter points near to the best of the previous optimization. The results are found to be robust to constraints and details of the fitting procedure. The uncertainties in the fit parameters are typically 2 μeV and are calculated by the delete-m jackknife method. The spectroscopy below the critical field of the Ti consistently contains a fixed normal metal component which we attribute to inhomogeneities in the Ti and incorporate into the model as detailed in Figure S6. Even at the lowest temperatures, the line-width of N_{Al} exceeds $k_B T$ to an extent attributable to gap anisotropy in Al[15]. This is accounted for in the model by uniformly convolving the N_{Al} with a normalized Gaussian of width 18 μeV for device 1 and 9 μeV for device 2. The simple convolution does not introduce significant error as compared to a more realistic model in which the gap is distributed uniformly according to the known gap anistropy in Al as shown in Figure

S7[29].

IV. ACKNOWLEDGEMENTS

We would like to acknowledge Pat Gumann for fruitful discussions. We are also grateful to Anthony Annunziata for his engagement and support. This work is supported by IBM Quantum, under Q Network for Academics program. This work is also partly supported by NSF grant DMR-1708688. LDA acknowledges support from an appointment to the Intelligence Community Postdoctoral Research Fellowship Program at Harvard University, administered by Oak Ridge Institute for Science and Education through an interagency agreement between the U.S. Department of Energy and the Office of the Director of National Intelligence.

V. AUTHOR CONTRIBUTIONS

LDA, AKS, CGB, ATP, SHL, and SPH performed low-temperature data acquisition. LDA and AKS fabricated the devices and performed the data analysis. LDA and AY designed the experiments. All authors contributed to interpreting the data and writing the manuscript.

---

[1] Levine, J. L. & Hsieh, S. Y. Recombination time of quasiparticles in superconducting aluminum. *Physical Review Letters* **20**, 994–997 (1968).

[2] Smith, L. N. & Mochel, J. M. Phonon and quasiparticle dynamics in superconducting aluminum tunnel junctions. *Physical Review Letters* **35**, 1597–1600 (1975).

[3] Ullom, J., Fisher, P. & Nahum, M. Measurements of quasiparticle thermalization in a normal metal. *Physical Review B* **61**, 14839–14843 (2000).

[4] Barends, R. *et al.* Quasiparticle relaxation in optically excited high-Q superconducting resonators. *Physical Review Letters* **100**, 257002 (2008).

[5] Patel, U., Pechenezhskiy, I. V., Plourde, B. L., Vavilov, M. G. & McDermott, R. Phonon-mediated quasiparticle poisoning of superconducting microwave resonators. *Physical Review B* **96**, 220501 (2017).

[6] Buck, D. A. The cryotron: a superconductive computer component. *Proceedings of the IRE* **44**, 482–493 (1956).

[7] Krinner, S. *et al.* Engineering cryogenic setups for 100-qubit scale superconducting circuit systems. *EPJ Quantum Technology* **6**, 2 (2019).

[8] Likharev, K. K. & Semenov, V. K. RSFQ logic/memory family: a new josephson-junction technology for sub-terahertz-clock-frequency digital systems. *IEEE Transactions on Applied Superconductivity* **1**, 3–28 (1991).

[9] McCaughan, A. N. & Berggren, K. K. A superconducting-nanowire three-terminal electrothermal device. *Nano Letters* **14**, 5748–5753 (2014). 1403.6423.

[10] Gray, K. E. A superconducting transistor. *Applied Physics Letters* **32**, 392–395 (1978).

[11] Bøttcher, C. G. *et al.* Superconducting, insulating and anomalous metallic regimes in a gated two-dimensional semiconductor–superconductor array. *Nature Physics* **14**, 1138–1144 (2018).

[12] Casparis, L. *et al.* Superconducting gatemon qubit based on a proximitized two-dimensional electron gas. *Nature Nanotechnology* **13**, 915–919 (2018).

[13] Glover, R. E. & Sherrill, M. D. Changes in superconducting critical temperature produced by electrostatic charging. *Physical Review Letters* **5**, 248–250 (1960).

[14] De Simoni, G., Paolucci, F., Solinas, P., Strambini, E. & Giazotto, F. Metallic supercurrent field-effect transistor. *Nature Nanotechnology* **13**, 802–805 (2018).

[15] Wolf, E. L. *Principles of Electron Tunneling Spectroscopy* (Oxford University Press, 2012), 2nd edn.

[16] Serniak, K. *et al.* Hot nonequilibrium quasiparticles in transmon qubits. *Physical Review Letters* **121**, 157701 (2018).

[17] Vepsäläinen, A. *et al.* Impact of ionizing radiation on superconducting qubit coherence. Preprint at: http://arxiv.org/abs/2001.09190 (2020).

[18] Li, L., Frunzio, L., Wilson, C. M. & Prober, D. E. Quasiparticle nonequilibrium dynamics in a superconducting Ta film. *Journal of Applied Physics* **93**, 1137–1141 (2003).

[19] Sapra, N. V. *et al.* On-chip integrated laser-driven particle accelerator. *Science* **367**, 79–83 (2020).

[20] Hauser, J. J. Enhancement of superconductivity in aluminum films. *Physical Review B* **3**, 1611–1616 (1971).

[21] Worledge, D. & Geballe, T. Maki analysis of spin-polarized tunneling in an oxide ferromagnet.

Physical Review B **62**, 447–451 (2000).

[22] Abrikosov, A. A. & Gorkov, L. P. Contribution to the theory of superconducting alloys with paramagnetic impurities. *JETP Letters* **39**, 1781 (1960).

[23] Tinkham, M. *Introduction to Superconductivity* (McGraw-Hill, New York, 1996), 2nd edn.

[24] Meservey, R. & Tedrow, P. M. Properties of very thin aluminum films. *Journal of Applied Physics* **42**, 51–53 (1971).

[25] Bi, C. *et al.* Reversible control of Co magnetism by voltage-induced oxidation. *Physical Review Letters* **113**, 267202 (2014).

[26] Kumar, P. *et al.* Origin and reduction of 1/f magnetic flux noise in superconducting devices. *Physical Review Applied* **6**, 041001 (2016).

[27] Jensen, K. *Introduction to the Physics of Electron Emission* (John Wiley & Sons, Hoboken, NJ, 2018).

[28] Hsieh, S. Y. & Levine, J. L. Diffusion of quasiparticles in superconducting aluminum films. *Physical Review Letters* **20**, 1502–1504 (1968).

[29] Blackford, B. L. A tunneling investigation of energy-gap anisotropy in superconducting bulk aluminum crystals. *Journal of Low Temperature Physics* **23**, 43–52 (1976).

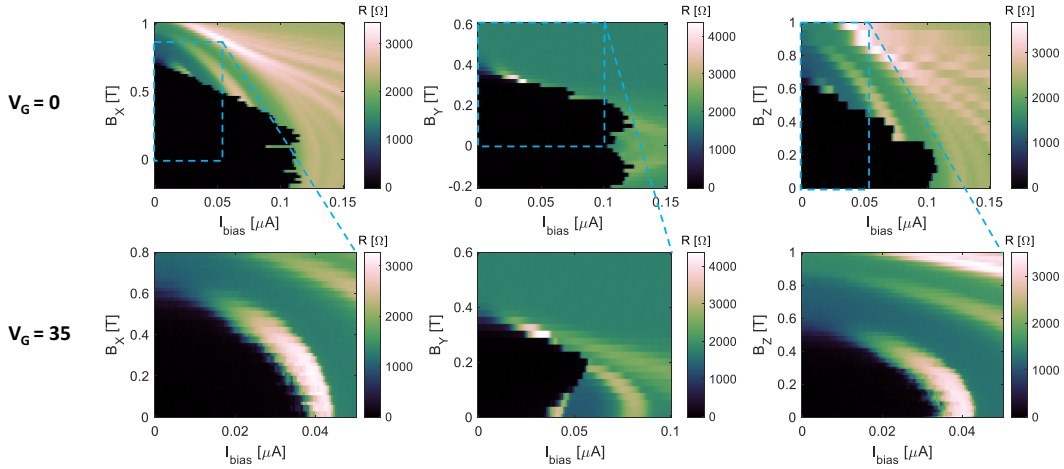

FIG. S1: Resistance of the Ti wire of Figure 1 as a function of magnetic field applied along x, y, z directions for zero applied gate voltage (top row) and 35 V (bottom row).

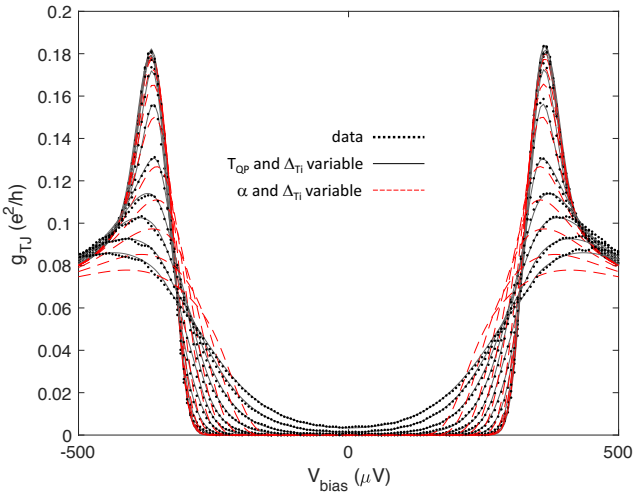

FIG. S2: Tunnel junction conductance vs bias data (dots) for gate voltages from 20 V (most peaked) to 43 V (least peaked) as compared to best fits with $T_{\rm QP}$ as free parameter (lines) and best fits with $\alpha_{\rm Al}$ as free parameter (dashed lines).

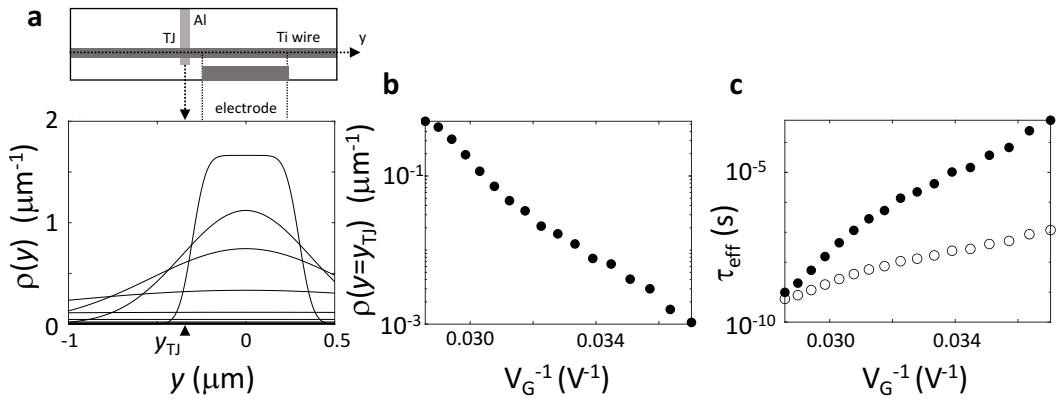

FIG. S3: The minimal model of quasiparticle dynamics presented in the main text does not account for diffusion of QP along the Ti wire, away from the injection region. Correcting this can account for the departure of the data from equation (5) as follows: We assume that the QP distribute along the length of the Ti wire according to $\rho(y)$ due to one-dimensional diffusion over a distance $(2D_{\rm Ti}\tau_{\rm eff})^{1/2}$ where $D_{\rm Ti}$ is the diffusion constant calculated from the magnetic field data. That is $\rho(y) = \rho_0 \int_{-l_I/2}^{l_I/2} \exp((s-y)^2/2D_{\rm Ti}\tau_{\rm eff})ds$ where ρ_0 is such that $\int \rho(y)dy = 1$, and l_I is the injector length. Moreover, we relax the assumption that $\tau_{\rm eff} \sim x_{\rm Ti}^{-1}$. The new model amounts to replacing A on the right hand side of equation (5) with $A\rho(y_{\rm TJ}, \tau_{\rm eff})x_{\rm Ti}\tau_{\rm eff}\Omega/(l_I t_{\rm TJ} w_{\rm TJ})$ where $y_{\rm TJ}$ is the distance from the tunnel junction to the center of the injection electrode, l_I is the length of the injection electrode, $t_{\rm TJ}$ is the thickness of the tunnel junction portion of the Ti wire, $w_{\rm TJ}$ is the width of that portion, and now $\tau_{\rm eff} = \tau_0 x^\nu$. The values $l_I = 600$ nm, $t_{\rm TJ} = 5$ nm, $w_{\rm TJ} = 7$ nm, and $\nu = 2.5$ correspond to the curved line in Figure 3f of the main text, which closely follows the data. However, the junction dimensions here are lower than expected, and a finite element model would be still more realistic. (a) $\rho(y)$ plotted at the relevant gate voltages, with the sharpest distribution corresponding to the highest voltage. (b) $\rho(y)$ evaluated at the location of the detector as a function of the gate voltages of Figure 3f. (c) The effective lifetime of quasiparticles implied by this model (filled circles) as compared to the minimal model described in the main text (open circles).

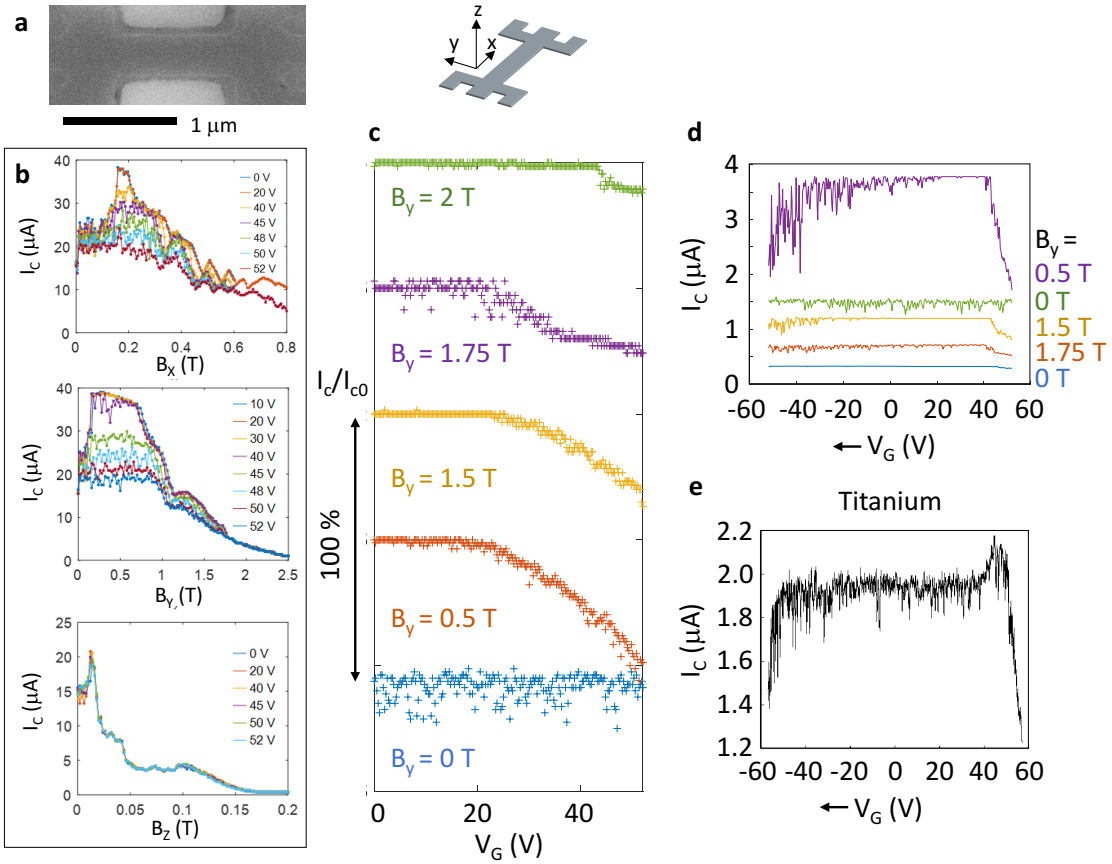

FIG. S4: Wide, back-gated critical current devices are measured at 50 mK in the geometry shown in (a). In a device composed of a 10 nm Al film on a 90 nm SiO_2 gate dielectric, the gate effect is observed only at elevated magnetic field. Critical current measurements are performed both at fixed gate voltage while sweeping magnetic field (b), or at fixed magnetic field while sweeping gate voltage (c). Oscillations observed at high B_x are likely to be related to Weber blockade and can be adjusted by the gate voltage. Hysteresis is observed in the gate effect, as can be seen in (d) in which the gate is swept from high to low voltage (over 20 minutes). A reversed behavior occurs when the gate is swept from low to high. (e) A similar Ti device shows a gate effect at zero magnetic field and the hysteresis takes the form of an overshoot of the gate effect (peak at positive V_G). The thickness of the Ti here is 30 nm.

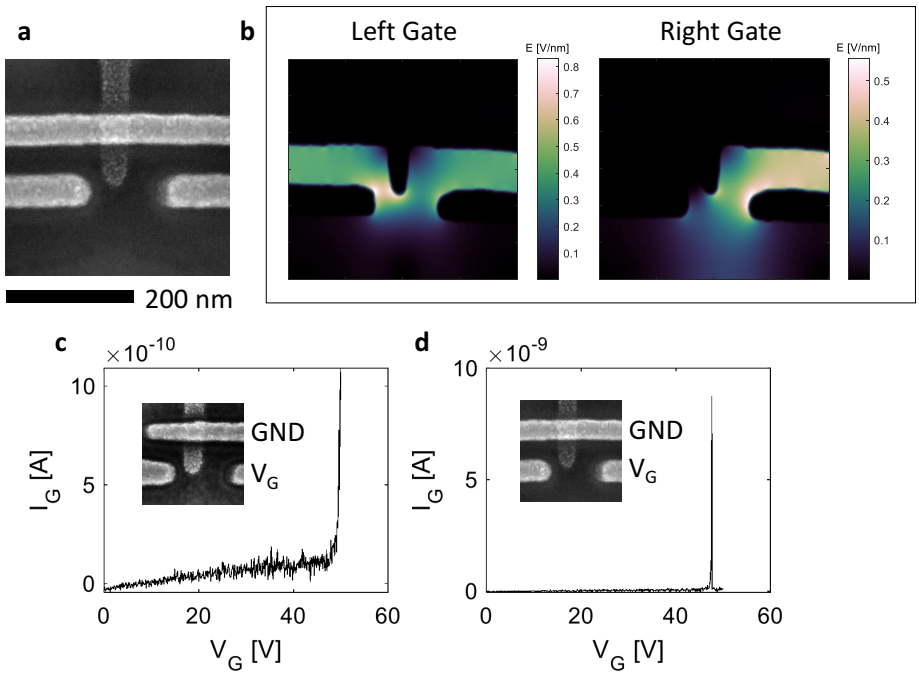

FIG. S5: Electric field calculation and current measurements. The device of the main text (a) has a slight asymmetry in the y-direction. As a result, the left and right gates produce different electric field distributions, the magnitude of which we calculate numerically in (b) for 40 V applied to either gate. As a result of this asymmetry, we use the right gate in the data of the main text, since this most effectively applies field to the Ti. (c) To look for current flow through the gate, we measure gate current in devices identical to the devices in the text, but at 4.2 K. We observe breakdown at 45 - 60 V in such devices, above the region of stable emission in the text. Below breakdown, the small amount of current detected is ohmic and almost certainly takes place in the contacts in this measurement. In the devices of Figure S4, measured in a separate dilution refrigerator with high line-isolation, current was measured to be less than 1 pA at for $V_G = 52$ V, but these devices had a different gate geometry (90 nm SiO_2 back gate). The Fowler-Nordheim model described in the main text predicts current of ~ 0.1 nA at the highest voltage.

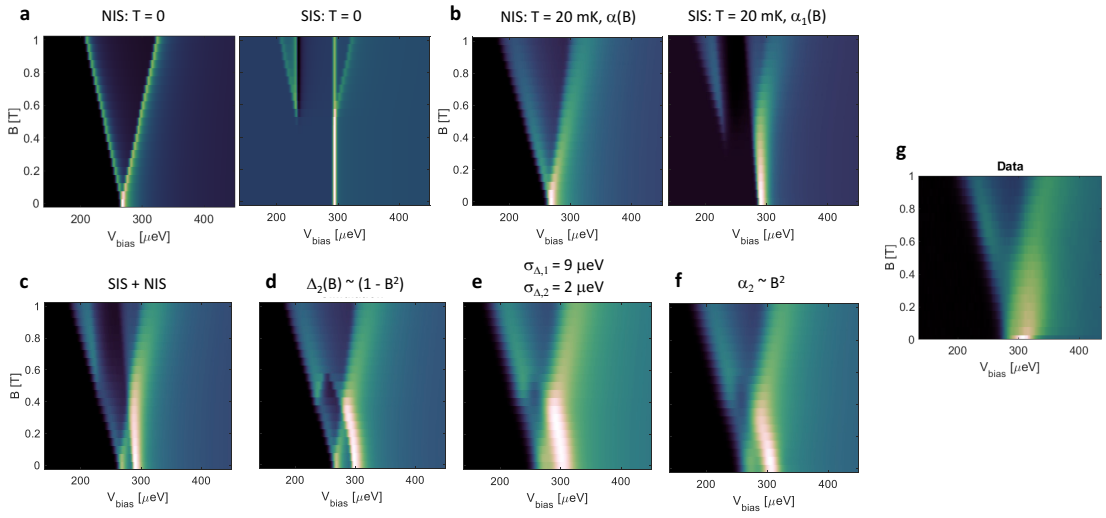

FIG. S6: (a) The magnetic field dependences of the normal metal-insulator-superconductor (NIS) and superconductor-insulator-superconductor (SIS) junctions have distinct signatures in magnetic field, since the spin subbands of the two layers of the SIS junction shift together in applied magnetic field. We illustrate the difference by simulating the effect of Zeeman splitting for a system of two films with large and small gap ($\Delta_1 > \Delta_2$) similar to the films in the main text but at zero $T_{\rm QP}$ and α. (b) Here we include 20 mK temperature and an estimated α_1. The absence of a significant difference-of-gap peak in the SIS spectrum at this temperature, and the absence of the Zeeman-split peak as in the NIS spectrum, strictly prevents the SIS model from fully explaining the current below the sum-of-gaps peak and below the critical field of film 2 which is observed in the data. (c) However, if we consider tunneling to occur into a normal metal portion of film 2 and add the contributions to the conductance, the general form of the data is well-captured. We consider this to be realistic given the susceptibility of Ti to oxidation. For example, a 20 nm wide Ti nanowire made similarly to the one discussed in the main text was found to be metallic but non-superconducting at 20 mK. If we now apply estimates for magnetic dependence of Δ_2 (d), intrinsic breadth of the density of states due to gap anisotropy (e), and field dependent α_2, the result (f), is similar in form to the observed data (g) and now explains the extra current below the sum-of-gaps.

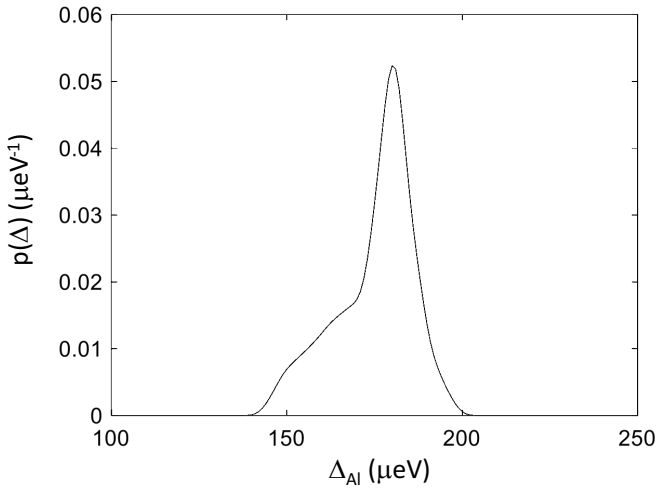

FIG. S7: The superconducting gap energy of Al plays an important role in the model presented in the main text. In a real sample, this value will be distributed due to crystalline anisotropy, as measured carefully in single-crystal Al samples by [29]. On the assumption that the line-width of $N_{\mathrm{Al}}(V_{\mathrm{bias}})$ reflects the underlying polycrystalline structure, we interpolate the data of [29] to calculate the distribution of gap energy $p(\Delta)$ assuming crystallites oriented randomly. Summing $N_{\mathrm{Al}}(V_{\mathrm{bias}})$ at all gap energies from this distribution produces a more accurate result, but we found that the effect on the results was negligible as compared to convolving $N_{\mathrm{Al}}(V_{\mathrm{bias}})$, for a fixed gap energy, with a Gaussian function. The latter calculation is far less computationally demanding and so was employed in the analysis to account for gap anistropy.